UCRL-JC-122408
PREPRINT
CONF-951182--5

The Evolution of Ultra-Intense, Short-Pulse Lasers in Underdense Plasmas

C. Decker
W. B. Mori
K-C. Tzeng
T. Katsouleas

This paper was prepared for submittal to the
37th Annual Meeting of the American Physical Society
Division of Plasma Physics
Louisville, KY
November 6-10, 1995

November 3, 1995

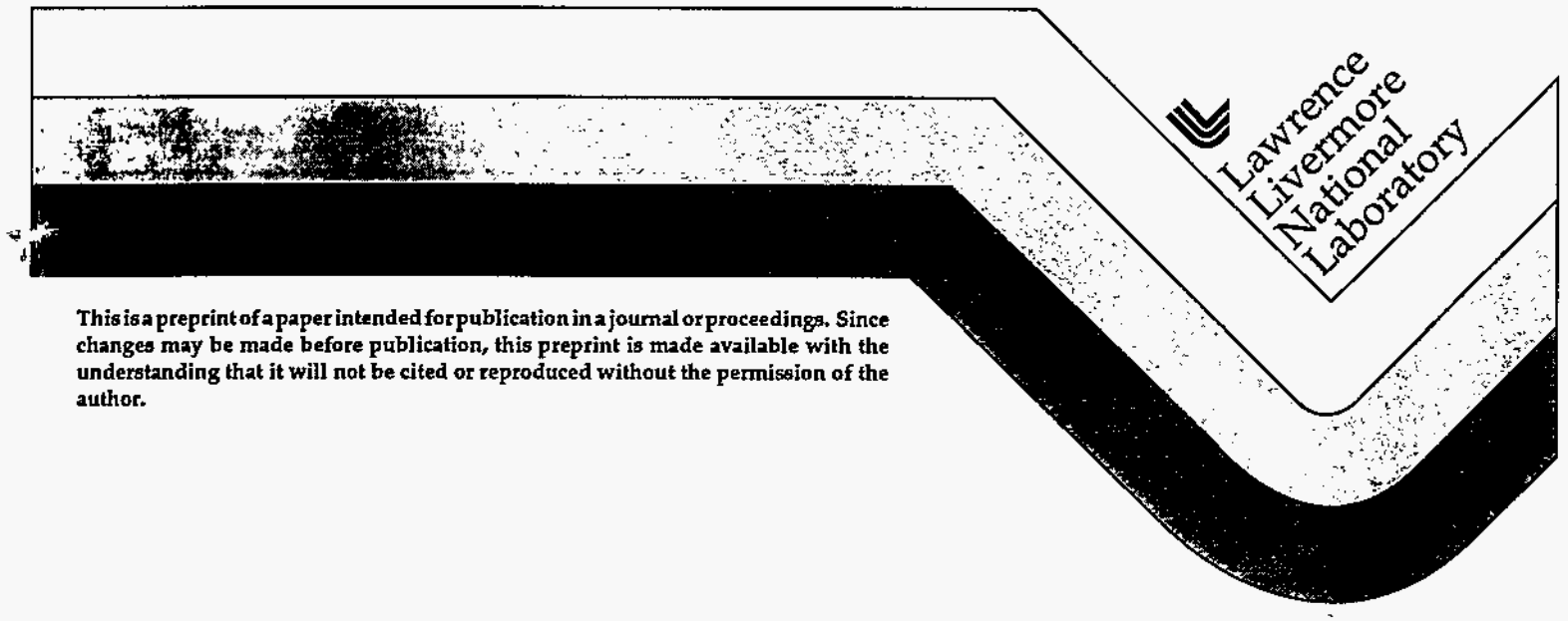

The Evolution of Ultra-Intense, Short-Pulse Lasers in Underdense Plasmas

C. D. Decker

Lawrence Livermore National Laboratory, Livermore, California 94550

W.B. Mori and K-C Tzeng

Departments of Physics and Electrical Engineering, University of California at Los Angeles

Los Angeles, California 90024

T. Katsouleas

Department Electrical Engineering, University of Southern California

Los Angeles, California 90089

The propagation of short-pulse lasers through underdense plasmas at ultra-high intensities ($I \geq 10^{19} W/cm$) is examined. The pulse evolution is found to be significantly different than it is for moderate intensities. Rather than beam breakup from self-modulation, Raman forward scattering and laser hose instabilities the behavior is dominated by leading edge erosion. A differential equation which describes local pump depletion is derived and used to analyze the formation and evolution of the erosion. This pulse erosion is demonstrated with one dimensional particle in cell (PIC) simulations. In addition, two dimensional simulations are presented which show pulse erosion along with other effects such as channeling and diffraction.

PACS number(s): 52.40.Nk, 52.35.Mw, 52.40.Db

I. INTRODUCTION

Recently, there has been several theoretical[1, 2, 3, 5, 4, 6] and experimental[7] investigations to determine the possibility of propagating short-pulse high-intensity lasers over extended distances through underdense plasmas. Throughout these studies it was shown that laser pulses of moderately high intensity ($I \leq 10^{18}$ W/cm) are susceptible to a variety of instabilities which cause the laser pulse to be absorbed and scattered in distances on the order of a Rayleigh length. These instabilities include Raman Backward, Forward[3] and Side Scattering[3, 8, 1], whole beam envelope self-modulation[5],laser hosing[6], relativistic self-phase modulation and relativistic self-focusing/filamentation[9]. It has been found[10] that a good indication of the nonlinear losses associated with these instabilities is the amount of Raman forward scattering within a Rayleigh length.

However, at ultra-high intensities($I \geq 10^{19}$ W/cm) the laser pulse evolution is both quantitatively and qualitatively different than it is for moderate intensities. Due to relativistic effects, the growth rates for the the above instabilities actually decreases at higher intensities. Therefore, these instabilities only disrupt the leading edge and have little effect on the main body of the pulse. This causes leading edge erosion. Another mechanism which can modify the front of the pulse is group velocity steepening. Regions of the pulse with larger amplitude have a larger group velocity[11] and overtake neighboring regions of lesser amplitude with slower group velocity. In either case, an ultra-intense laser pulse always forms a steepened front. Once this steeped front has developed, it ponderomotively excites a large amplitude plasma wave wake which leads to further erosion. The laser pulse quickly evolves to a state in which the leading edge excites large amplitude plasma waves and density perturbations while continuously eroding backwards.

In this paper, we consider in detail the mechanisms that cause the formation and evolution of the steepened front. In the first section, we examine Raman scattering for

arbitrary pump strength. We derive a dispersion relation from which temporal growth rates can be found. Using these growth rates we show that the whole beam instabilities mentioned above are ineffective at breaking up or modifying the pulse significantly. In the next section, we turn our attention to the localized pump depletion caused by a sharp front. We present a Lagrangian density function from which we can derive local conservation laws. Using these conservation laws we derive an expression for the local depletion of laser energy. From this local pump depletion equation we can identify the terms responsible for energy transport and energy loss. The rate at which the pulse erodes once the sharp front has formed is estimated from this equation and the conditions for 100 percent local pump depletion are given. In order to quantify the formation of the front we next examine Raman scattering at ultra-high intensities and use the growth rates to estimate the formation time. Next, we present one dimensional(1-D) PIC simulations which demonstrate this leading edge erosion and two dimensional(2-D) simulations which show additional effects such as ponderomotive electron expulsion, local diffraction and laser pulse bullet formation. Lastly, the consequences and possible application of this behavior are briefly discussed

III. RAMAN SCATTERING AT ULTRA-HIGH INTENSITIES

Recently, it has been shown[10] that Raman forward scattering at forward and near forward angles is one of the most disruptive instabilities at moderately high intensities. In addition, it has also been shown[12] that self-modulation[5] and laser hosing[6] are related to Raman scattering in the same way that self-focusing is related to filamentation. That is, self-modulation and laser hosing are whole beam analogs of plane wave Raman scattering at forward and near forward angles. Therefore, examining Raman scattering at the ultra-high intensities is important for determining beam stability. In this section we extend the analysis for one dimensional Raman scattering to include arbitrarily large pump intensities. We do this by perturbing a nonlinear equilibrium solution with a small amplitude plasma wave and small amplitude stokes and anti-stokes waves. We start with the fully nonlinear wave equation for the radiation in slab geometry

$$\left(\frac{\partial^2}{\partial t^2} - c^2\frac{\partial^2}{\partial x^2}\right)\vec{a} = -\frac{\omega_p^2}{n_o}\frac{n}{\gamma}\vec{a} \tag{1}$$

the continuity equation

$$\frac{\partial n}{\partial t} + \frac{\partial}{\partial x}\left(\frac{np}{m\gamma}\right) = 0 \tag{2}$$

and the electron momentum equation

$$\frac{\partial p}{\partial t} = -eE_{\|} - mc^2\frac{\partial \gamma}{\partial x} \tag{3}$$

where $\vec{a} = e\vec{A}/mc^2$ is the normalized vector potential, n is the electron density, p is the electron momentum in the x direction and $\gamma^2 = 1+a^2+p^2/m^2c^2$. Unlike the case of a small amplitude pump, the polarization of the pump is very important for finite amplitude. The only exact transverse solution is for circular polarization. Linearly polarized waves have odd harmonics of the vector potential and even harmonics of the density which can

couple to the plasma wave. Therefore, the nonlinear solution is not purely transverse. For simplicity we first consider circularly polarized light. We note that we have carried out the analysis[13] for linear polarization and the results are unchanged in so far as the growth rates are concerned.

The equilibrium solution for a circularly polarized electromagnetic wave is of the form

$$\vec{a}_p = \frac{\vec{a}_o}{2} e^{i\theta_o} + c.c. \tag{4}$$

Where $\theta_o = k_o x - \omega_o t$ and $\vec{a}_o = a_o(\hat{z} + i\hat{y})$. The nonlinear dispersion relationship is well known[14] $\omega_o^2 = c^2 k_o^2 + \frac{\omega_p^2}{\gamma_o}$ where $\gamma_o^2 = 1 + a_o^2$, $\omega_p^2 = \frac{4\pi n_o e^2}{m}$ and n_o is the unperturbed electron density. We note that this dispersion relation is exact for circularly polarized light. There is no longitudinal momentum associated with this wave and the density is constant. Circular polarization implies $\vec{a}_o \cdot \vec{a}_o = \vec{a}_o^* \cdot \vec{a}_o^* = 0$ and this is why circular polarization does not generate second harmonic density perturbation.

We perturb this equilibrium with a plasma wave described by the amplitude δn and an associated longitudinal momentum δp which are of the form

$$\delta n = \frac{n_1}{2} e^{i\theta} + c.c. \tag{5}$$

and

$$\delta p = \frac{p_1}{2} e^{i\theta} + c.c. \tag{6}$$

where $\theta = kx - \omega t$. This plasma wave beats with the pump generating electromagnetic sidebands of the form

$$\delta\vec{a} = \frac{a_-}{2} e^{i\theta_-} + \frac{a_+}{2} e^{i\theta_+} + c.c. \tag{7}$$

where $\theta_\pm = \theta \pm \theta_o$.

In order to evaluate the current source term $\frac{n}{\gamma}\vec{a}$ we first expand γ. The total relativistic γ factor of the pump and the perturbation is given by

$$\gamma^2 = 1 + a_p^2 + 2\vec{a}_p \cdot \delta\vec{a} + \delta a^2 + \delta p^2 \tag{8}$$

Likewise the total density is $n = n_o + \delta n$. Here we make the usual assumption that all perturbed quantities are on the order of some small parameter ϵ. In particular, we assume δn , δp and $\delta\vec{a}$ are all $O(\epsilon)$. We expand $\frac{1}{\gamma}$ to lowest order in ϵ to get

$$\frac{1}{\gamma} \simeq \frac{1}{\gamma_o}\left(1 - \frac{\vec{a}_p \cdot \delta\vec{a}}{\gamma_o^2}\right) \tag{9}$$

Likewise, to lowest order in ϵ, the current source term can now be written as

$$\frac{n}{\gamma}\vec{a} = \frac{n_o}{\gamma_o}\left(\delta\vec{a} + \frac{\delta n}{n_o}\vec{a}_p - \frac{(\vec{a}_p \cdot \delta\vec{a})}{\gamma_o^2}\vec{a}_p\right) \tag{10}$$

We first look for the terms of Eq. (10) that drive the stokes(θ_-) wave. Therefore, we substitute Eqs.(4),(5) and (6) into Eq. (10) and collect all terms that are proportional to $e^{i\theta_-}$. The result is

$$\left(\frac{n}{\gamma}\vec{a}\right)_{\theta_-} = \frac{1}{\gamma_o}\frac{n_1 a_o^*}{4} + \frac{n_o}{\gamma_o}\frac{a_-}{2} - \frac{n_o}{\gamma_o^3}(\vec{a}_o \cdot \vec{a}_-)\frac{\vec{a}_o^*}{8} - \frac{n_o}{\gamma_o^3}(\vec{a}_o^* \cdot \vec{a}_+)\frac{\vec{a}_o^*}{8} \tag{11}$$

Therefore, the stokes wave has the polarization of $\vec{a}_o^*$, and it can be shown that the anti-stokes has the polarization of $\vec{a}_o$. Therefore, the stokes wave can then be written as $\vec{a}_- = a_-(\hat{z} - i\hat{y})$ and the anti-stokes wave can be written as $\vec{a}_- = a_-(\hat{z} + i\hat{y})$. This implies that $\vec{a}_- \cdot \vec{a}_o^* = \vec{a}_+ \cdot \vec{a}_o = 0$. Furthermore, without loss of generality, we can set the phase of the pump so that $a_o = a_o^*$.

The wave equation for the stokes wave is then given by

$$\left(\frac{\partial^2}{\partial t^2} - c^2\frac{\partial^2}{\partial x^2} - \frac{\omega_p^2}{\gamma_o}\right) a_- e^{i\theta_-} = \left[\frac{\omega_p^2}{\gamma_o}\frac{n_1 a_o^*}{2n_o} - \frac{\omega_p^2}{4\gamma_o^3}a_o^2(a_- + a_+)\right] e^{i\theta_-} \tag{12}$$

and likewise the equation for the anti-stokes(θ_+) is then

$$\left(\frac{\partial^2}{\partial t^2} - c^2\frac{\partial^2}{\partial x^2} - \frac{\omega_p^2}{\gamma_o}\right) a_+ e^{i\theta_+} = \left[\frac{\omega_p^2}{\gamma_o}\frac{n_1 a_o}{2n_o} - \frac{\omega_p^2}{4\gamma_o^3}a_o^2(a_- + a_+)\right] e^{i\theta_+} \tag{13}$$

Next, we turn our attention to the plasma wave. We expand the second term on the right hand side of Eq. (2) to obtain

$$\left(\frac{n\vec{p}}{m\gamma}\right) = \frac{n_o}{m\gamma_o}\left(1+\frac{\delta n}{n_o}\right)\left(1-\frac{\vec{a}\cdot\delta\vec{a}}{\gamma_o^2}-\frac{\vec{a}\cdot\vec{p_1}}{\gamma_o^2}\right)\vec{p} \tag{14}$$

and to lowest order, Eq. (2) becomes

$$\frac{\partial n_1}{\partial t}+\frac{\partial}{\partial x}\left(\frac{n_o\vec{p_1}}{m\gamma_o}\right)=0 \tag{15}$$

Differentiating Eq. (15) with time and using Eq. (3) along with Gauss's law, gives

$$\left(\frac{\partial^2}{\partial t^2}+\frac{\omega_p^2}{\gamma_o}\right)\delta n = -\frac{n_o c^2}{\gamma_o}\frac{\partial^2\gamma}{\partial x^2} \tag{16}$$

We look for terms in Eq. (16) that are proportional to $e^{i\theta}$ Keeping terms at θ, we find an equation for the evolution of the plasma wave

$$\left(\frac{\partial^2}{\partial t^2}+\frac{\omega_p^2}{\gamma_o}\right)n_1 e^{i\theta} = -\frac{n_o c^2 k^2}{4\gamma_o^2}\left(\vec{a}_-\cdot\vec{a}_o+\vec{a}_+\cdot\vec{a}_o^*\right)e^{i\theta} \tag{17}$$

Eqs.(12), (13) and (17) completely describe Raman scattering for arbitrarily large pump amplitude. They not only describe describe Raman back and forward scattering, but also the relativistic modulational instability[15]. These regimes can easily be identified by deriving a dispersion relationship and evaluating the temporal growth rates. Here we assume that the amplitudes of the perturbations n_1,p_1 and $a_\pm$ are constant but the frequency ω and wave number k are complex. After Fourier analyzing, Eqs. (12),(13) and (17) become respectively,

$$\left(\omega_-^2-c^2k_-^2-\frac{\omega_p^2}{\gamma_o}\right)a_- = \frac{\omega_p^2}{\gamma_o}\frac{n_1 a_o^*}{2n_o}-\frac{\omega_p^2}{4\gamma_o^3}a_o^2\left(a_-+a_+\right) \tag{18}$$

$$\left(\omega_+^2-c^2k_+^2-\frac{\omega_p^2}{\gamma_o}\right)a_+ = \frac{\omega_p^2}{\gamma_o}\frac{n_1 a_o}{2n_o}-\frac{\omega_p^2}{4\gamma_o^3}a_o^2\left(a_-+a_+\right) \tag{19}$$

$$\left(\omega^2-\frac{\omega_p^2}{\gamma_o}\right)n_1 = \frac{n_o c^2 k^2}{2\gamma_o^2}\left(\vec{a}_+\cdot\vec{a}_o+\vec{a}_+\cdot\vec{a}_o^*\right) \tag{20}$$

Substituting Eq. (20) into Eqs. (18) and (19) gives

$$d_- a_- = d(a_- + a_+) \tag{21}$$

and

$$d_+ a_+ = d(a_- + a_+) \tag{22}$$

where

$$d_\pm = \omega_\pm^2 - c^2 k_\pm^2 - \frac{\omega_p^2}{\gamma_o} \tag{23}$$

and

$$d = \frac{\omega_p^2}{4\gamma_o^3} a_o^2 \left(\frac{c^2 k^2}{\omega^2 - \frac{\omega_p^2}{\gamma_o}} - 1 \right) \tag{24}$$

From Eq. (22) we find $a_+ = \frac{d}{d_+ - d} a_-$ and we substitute this into Eq. (21) to obtain a dispersion relation for arbitrary pump amplitude

$$1 = \frac{a_o^2 \omega_p^2}{4\gamma_o^3} \left(\frac{c^2 k^2}{\omega^2 - \frac{\omega_p^2}{\gamma_o}} - 1 \right) \left(\frac{1}{d_+} + \frac{1}{d_-} \right) \tag{25}$$

We note that we recover the well known small pump Raman dispersion relation[15] if we let $\gamma_o = 1$. From Eq. (25) we can examine the temporal growth rate of Raman Backscattering[16], Raman forward scattering and relativistic self modulation[9]. Using the pump dispersion $\omega_o^2 = c^2 k_o^2 + \frac{\omega_p^2}{\gamma_o}$ we can write $d_\pm = \omega^2 \pm 2(\omega_o \omega - c^2 k k_o) - c^2 k^2$. By comparing Eq. (25) with the small pump Raman dispersion relationship it is obvious that we can obtain the large pump amplitude growth rates from the well known small amplitude growth rates[16, 15] by simply rescaling $a_o^2 \to \frac{a_o^2}{\gamma_o^2}$ and $\omega_p^2 \to \frac{\omega_p^2}{\gamma_o}$.

First we examine the temporal growth rate for Raman backscattering which is a 3-wave process in which the stokes wave propagates anti-parallel to the pump. The growth rate for small pump amplitude is well know[16] and given by given by $\nu_{srs} = \frac{a_o}{4}\sqrt{\omega_o \omega_p}$. Therefore, rescaling a_o and ω_p immediately gives the large pump Raman backscattering

growth rate

$$\Gamma_{rbs} = \frac{\sqrt{\omega_o \omega_p}}{4} \frac{a_o}{\gamma_o^{5/4}} \tag{26}$$

We note that as $a_o \rightarrow \infty$ the growth rate $\Gamma_{rbs} \sim a_o^{-1/4}$. If $\Gamma_{rbs} > \omega_p/\gamma_o$ then the instability is in a strongly-coupled backscatter[16] regime. The small pump this growth rate is given by $\nu_{scb} = \sqrt{3}\left(\frac{\omega_o \omega_p^2}{16}\right)^{1/3}$ while, the large pump growth rate for strongly coupled raman backscatter is given by

$$\Gamma_{scb} = \sqrt{3}\left(\frac{\omega_o \omega_p^2}{16}\right)^{1/3} \frac{a_o^{2/3}}{\gamma_o} \tag{27}$$

The strongly-coupled growth rate was obtained previously by others[17, 5]. We note that as $a_o \rightarrow \infty$ $\nu_{scb} \sim a_o^{-1/3}$ and ν_{scb} has a maximum at $a_o = 2$. The asymptotic reduction in the Raman backscattering growth rate is due to the difficulty in causing relativistic electrons to oscillate.

The small pump growth rate for Raman forward scattering is given by $\nu_o = \frac{a_o \omega_p^2}{\sqrt{8}\omega_o}$. Rescaling this growth rate we obtain the large pump growth rate

$$\Gamma_{rfs} = \frac{1}{\sqrt{8}} \frac{\omega_p^2}{\omega_o} \frac{a_o}{\gamma_o^2} \tag{28}$$

We note that as $a_o \rightarrow \infty$ the growth rate $\nu_{rfs} \sim a_o^{-1}$. The physical reason can be attributed to the relativistic mass increase of the quivering electrons. The ponderomotive force is proportional to $\frac{1}{\gamma_o}\nabla a_o^2 = \frac{1}{\gamma_o} k a_o^2$. Since the phase velocity is close to c $k = \omega$ and $\omega = \omega_p^2/\gamma_o$, then as a result of the relativistic mass increase there is a reduction in the ponderomotive force.

The relativistic modulational instability differs from Raman forward scattering in that the low frequency modes, i.e., the idler is not a plasma wave. For this case $\omega \approx k \ll \frac{\omega_p}{\gamma_o^{1/2}}$ It is dominant when $c^2 k^2 \ll \omega^2 - \frac{\omega_p^2}{\gamma_o}$. The weakly relativistic growth rate is known to be[9] $\nu_{rmi} = \frac{a_o^2 \omega_p^2}{8\omega_o}$. The large amplitude extension is therefore

$$\Gamma_{rmi} = \frac{\omega_p^2}{8\omega_o} \frac{a_o^2}{\gamma_o^3} \tag{29}$$

So far we have derived temporal growth rates for Raman back and forward scattering. For short pulse interactions the instability is in a spatial-temporal regime[3]. However, the spatial-temporal solutions[12] always involve the temporal growth rates. In particular, the amount of exponetiation (number of e-foldings) for Raman forward scattering at a given position ξ in the pulse after a time τ is given by[3]

$$G = \Gamma_{rfs}\sqrt{(\tau - \xi/c)\xi/c} \tag{30}$$

For example, we consider a $\xi/c = 100$ fsec pulse propagating through a $4 \times 10^{19} W/cm^2$ plasma. We use Eq. (30) to determine the number of e-foldings after a pulse has propagated a Rayleigh length. We take a typical spot size of 20 microns which gives a Raleigh time of $\tau = 4.2$ psec. For an intensity of $10^{20} W/cm$ the number of e-foldins is just 1.74 which too small to see any beam break up or other effects of Raman forward scattering[4].

II. LOCAL PUMP DEPLETION EQUATIONS

Since pulse erosion is a localized phenomena, we need to derived localized pump depletion equations. In order to derive pump depletion equations we make use of the quasi-static approximation. The quasi-static equations [18] are a fully nonlinear set of coupled equations for the scalar potential Φ and the vector potential $\vec{A}$. They are derived from the fully nonlinear fluid equations and the nonlinear wave equation for $\vec{A}$. The quasi-static approximation consists of neglecting $\frac{\partial}{\partial \tau}$ in the continuity equation and in the longitudinal equation of motion after a mathematical transformation has been made from the (x,t) to the $(\xi = x - ct, \tau = t)$ coordinates. The quasi-static equations for the normalized potentials $\phi = e\Phi/mc^2$ and $\vec{a} = e\vec{A}/mc^2$ are given by

$$\left(\frac{2}{c}\frac{\partial^2}{\partial\xi\partial\tau} - \frac{1}{c^2}\frac{\partial^2}{\partial\tau^2}\right)\vec{a} = k_p^2\frac{\vec{a}}{1+\phi} \tag{31}$$

and

$$\frac{\partial^2}{\partial\xi^2}\phi = \frac{1}{2}k_p^2\left(\frac{1+a^2}{(1+\phi)^2} - 1\right) \tag{32}$$

where $k_p = \omega_p/c$

Eqs. (31) and (32) completely describe the nonlinear laser plasma interaction and predict leading edge erosion. However, Eqs. (31) and (32) can be derived form the following Lagrangian density function

$$\mathcal{L}(\vec{a}, \vec{a}_\xi, \vec{a_\tau}, \phi, \phi_\xi) = \frac{1}{2}\phi_\xi^2 + \frac{1}{2c^2}a_\tau^2 - \frac{1}{c}\vec{a}_\xi \cdot \vec{a}_\tau - \frac{k_p^2}{2}\left[\frac{1+a^2}{1+\phi} + \phi - 1\right] \tag{33}$$

where the subscripts ξ and τ denote $\frac{\partial}{\partial\xi}$ and $\frac{\partial}{\partial\tau}$ respectively. Verifying that this is the Lagrangian density is easily done by showing that $\frac{\partial\mathcal{L}}{\partial a} - \frac{\partial}{\partial\tau}\frac{\partial\mathcal{L}}{\partial a_\tau} - \frac{\partial}{\partial\xi}\frac{\partial\mathcal{L}}{\partial a_\xi}$ and $\frac{\partial\mathcal{L}}{\partial\phi} - \frac{\partial}{\partial\tau}\frac{\partial\mathcal{L}}{\partial\phi_\tau} - \frac{\partial}{\partial\xi}\frac{\partial\mathcal{L}}{\partial\phi_\xi}$ recovers Eqs. (31) and (32). A Lagrangian density is useful because differential, i.e., local, rather than integral conservation equations can be easily derived.

The conservation equations are obtained by taking the divergence of the stress-energy tensor of the system [19]. The resulting conservation equations are

$$\frac{\partial}{\partial\tau}\left(\frac{1}{2c^2}a_\tau^2-\frac{1}{2}\phi_\xi^2+\frac{k_p^2}{2}\left[\frac{1+a^2}{1+\phi}+\phi-1\right]\right)+\frac{\partial}{\partial\xi}\left(\phi_\xi\phi_\tau-\frac{1}{c}a_\tau^2\right)=0 \qquad (34)$$

and

$$\frac{\partial}{\partial\tau}\left(\frac{1}{c^2}\vec{a}_\tau\cdot\vec{a}_\xi-\frac{1}{c}a_\xi^2\right)+\frac{\partial}{\partial\xi}\left(\frac{1}{2}\phi_\xi^2-\frac{1}{2c^2}a_\tau^2+\frac{k_p^2}{2}\left[\frac{1+a^2}{1+\phi}+\phi-1\right]\right)=0 \qquad (35)$$

Eq. (35) is the most useful because the left hand term of Eq. (35) is the rate of change in the transverse electromagnetic energy, $\mathcal{E}_\perp \equiv \frac{E_\perp^2+B_\perp^2}{8\pi}/n_o mc^2$. To verify this, we use the relationships $\vec{E}_\perp = -\frac{1}{c}\frac{\partial\vec{A}}{\partial t}$ and $\vec{B}_\perp = \frac{\partial\vec{A}}{\partial z}$ along with $\frac{\partial}{\partial t} = \frac{\partial}{\partial\tau} - c\frac{\partial}{\partial\xi}$ and $\frac{\partial}{\partial z} = \frac{\partial}{\partial\xi}$ to show that

$$\mathcal{E}_\perp = \frac{c^2}{2\omega_p^2}\left(\frac{1}{c^2}a_\tau^2-\frac{2}{c}\vec{a}_\tau\cdot\vec{a}_\xi+2a_\xi^2\right) \qquad (36)$$

In the quasi-static approximation, it is assumed that $\frac{\partial\vec{a}}{\partial\tau} \ll \frac{\partial\vec{a}}{\partial\xi}$, so a_τ^2 can be neglected in Eq. (36) and Eq. (35) can be rewritten as

$$\frac{1}{c}\frac{\partial}{\partial\tau}(\mathcal{E}_\perp)-\frac{\partial}{\partial\xi}\left(\frac{1}{2k_p^2}\chi_\xi^2+\frac{1}{2}\left[\frac{1+a^2}{\chi}+\chi-1\right]\right)=0 \qquad (37)$$

where $\chi = 1+\phi$.

Eq. (37) is of the form $\frac{\partial}{\partial\tau}\mathcal{E}_\perp + \frac{\partial}{\partial\xi}S = 0$ and describes the evolution of perpendicular(laser) energy. The local value of $\mathcal{E}_\perp$ can change by energy convecting out of (or into) the local region or it can change by conversion to longitudinal energy (pump depletion). We note that when pump depletion is absent, i.e. $\frac{\partial}{\partial\tau}\int_{-\infty}^{\infty}\mathcal{E}_\perp = 0$, there is only energy transport and Eq.(37) can be used to define a local energy transport velocity or group velocity[11] $v_g = \frac{<S>}{<\mathcal{E}_\perp>}$ where $<>$ represents averaging over the fast oscillations of the laser.

We want to separate the terms responsible for energy transport and the terms responsible for energy loss. If there is a contribution S_1 to the energy flux $S = S_1 + S_2$ such

that $\int_{-\infty}^{\infty} \frac{\partial S_1}{\partial \xi} d\xi = 0$ then S_1 does not contribute to pump depletion. It can be shown that the $\frac{1+a^2}{\chi} + \chi - 1$ term in Eq. (37) satisfies this criteria. Therefore, if we write Eq. (37) in the form

$$\frac{1}{c}\frac{\partial}{\partial \tau}\mathcal{E}_\perp + \frac{\partial}{\partial \xi}(v_g \mathcal{E}_\perp) = \frac{1}{2}\frac{\partial}{\partial \xi}E_\parallel^2 \tag{38}$$

where the normalized group velocity[11] in this frame is $v_g = -\frac{k_p^2}{2}\left(\frac{1+a^2}{\chi} + \chi - 1\right)/\mathcal{E}_\perp$ and the normalized longitudinal electric field is $E_\parallel = -\frac{1}{k_p}\frac{\partial \chi}{\partial \xi}$. The importance of Eq. (38) is that we can identify $\frac{\partial}{\partial \xi}E_\parallel^2$ as the pump depletion term. We note that using Eqs. (31) and (32), Eq. (38) can be written as $\frac{1}{c}\frac{\partial}{\partial \tau}\mathcal{E}_\perp = \frac{1}{2\chi}\frac{\partial a^2}{\partial \xi}$. An integral form of this has been derived by others[17]. However, integral equations are not useful when analyzing localized erosion.

We see that if $\frac{\partial}{\partial \xi}E_\parallel^2$ is localized then the pump depletion will also be localized. For short intense laser pulses the plasma wave wake becomes nonlinear and wave steepening results in $\frac{\partial}{\partial \xi}E_\parallel^2$ becoming localized. For pulses with durations longer than a plasma period no substantial wake is formed. However, Raman backscattering and Raman forward scattering, which grow from the front of the pulse to the back, can saturate in very short distances. We find that Raman back and forward scattering depletes energy locally creating a small notch in the laser pulse. This notch ponderomotively excites a wake further depleting the pulse's energy. Eventually the term $\frac{\partial}{\partial \xi}E_\parallel^2$ becomes even more localized until a sharp front is formed.

To determine under what conditions pump depletion is localized, we examine the $\frac{\partial}{\partial \xi}E_\parallel^2$ term. It is useful to rewrite it as $\frac{1}{2k_p}\frac{\partial}{\partial \xi}E_\parallel^2 = -E_\parallel \delta n$ where δn is the perturbed electron density normalized to n_o. We restrict the analysis to square shaped leading edges because, as we will show in the simulations, this is the eventual state of the laser pulse. In addition, we consider circular polarization because exact solutions to Eq. (32) can be found[20]. Using Eq. (32) we can find $\delta n = \frac{1}{k_p^2}\frac{\partial^2 \phi}{\partial \xi}$. For a given value of a at the

head of the pulse the maximal values of δn and $E_{\|}$ are given by[20]

$$|\delta n| = \frac{a^2}{2} \tag{39}$$

and

$$E_{\|} = \sqrt{1+a^2}\ . \tag{40}$$

The full width half maximum of the density spike, ΔL, can be estimated from Gauss's law

$$\Delta L = \frac{1}{2}\frac{E_{\|}}{\delta n} \approx \frac{\sqrt{1+a^2}}{a^2} \approx \frac{1}{a} \tag{41}$$

This width is narrow if $a \gg 1$. That is why local pump depletion only occurs for $I\lambda^2 \geq 10^{19} W/cm^2 \cdot \mu m$. We can estimate the etching velocity by dividing ΔL by the time is takes to completely deplete the laser energy within the density spike.

$$\Delta\tau = \frac{\mathcal{E}_{\perp}}{E_{\|}\delta n} \tag{42}$$

Therefore,

$$v_{etch} = \frac{\Delta L}{\Delta\tau} = \frac{1}{2}\frac{E_{\|}^2}{\mathcal{E}_{\perp}} = \frac{E_{\|}^2}{E_{\perp}^2} = \frac{\omega_p^2}{\omega_o^2} \tag{43}$$

However, the velocity of the leading edge is the linear group velocity minus v_{etch} so the front velocity is

$$v_f \simeq 1 - \frac{1}{2}\frac{\omega_p^2}{\omega_o^2} - \frac{\omega_p^2}{\omega_o^2} \simeq 1 - \frac{3}{2}\frac{\omega_p^2}{\omega_o^2} \tag{44}$$

This agrees reasonably well with the simulation results presented in the next section. We comment that in Ref.[21] the formation of shocks was analyzed and they obtained a shock velocity similar to Eq. (44) except that the coefficient was 1.22 instead of 3/2. However, they made assumptions which are not consistent with the observations in the simulations. The etching of the front also prevents the diffraction of the leading edge as described by Sprangle et al.[18]. To lowest order, the front c/ω_p of a pulse diffracts in a Raleigh length. Therefore, the local depletion of the front dominates diffraction if

$\sigma^2 > 2\frac{\omega_o}{\omega_p}\frac{c^2}{\omega_p^2}$ where σ^2 is the Gaussian spot size. This criteria can easily be satisfied for near-term lasers

Since the etch velocity is less than the group velocity, the pulse can entirely erode after propagating some finite distance. This time is determined form the condition $(v_g - v_{etch})t = L$ where L is the pulse length of the laser. For example, a 100 fsec pulse propagating through a $4 \times 10^{19}\text{cm}^{-3}$ plasma completely erodes after propagating just 0.75 mm.

IV. SIMULATIONS

Pump depletion was investigated using the electromagnetic particle-in-cell codes WAVE[22] and PEGASUS[7]. WAVE is used because is solves for the vector and scalar potentials which prove to be useful whereas PEGASUS is used because it runs on parallel computers, and therefore, can simulate large systems. These simulations are done in the x-y plane with linear polarization in the z direction. Radiation is launched from the left hand boundary and propagates in the x direction into the plasma.

We first present a 1-d WAVE simulation to demonstrate the formation and evolution of the sharp front. The parameters chosen were $a_o = 10.0$, $\omega_o/\omega_p = 5.0$ and a FWHM pulse length of $l_o = 125c/\omega_o$ which for a $1\mu m$ laser correspond to an $1.4\times10^{20}W/cm^3$, $60fs$ pulse propagating through a $n_o = 4 \times 10^{19}cm^{-3}$ plasma. The system size is $x_{max} = 500c/\omega_o$. In Fig. 1 we plot the transverse electric field associated with the laser for $ct = 0.08$, 0.16, 0.24 and 0.32 mm. To illustrate the details of the pulse erosion we only plot the region around the pulse as it propagates through the simulation box, i.e., a moving window. We see that after only propagating 0.08 mm the front of the laser pulse has started to deplete. Analysis of the backscattered radiation indicates that the erosion was primarily due to Raman backscattering. The backscattered radiation grew very rapidly and its Fourier spectrum was appropriately downshifted. We note that group velocity steepening may have also played a role in the initial formation of the steep front. However, it is not as easy to diagnose as Raman backscattering. Once the sharp front is formed the pulse continuously etches backward. The velocity of the front from this simulation is found to be $(1 - v_f)\frac{\omega_o^2}{\omega_p^2} = 1.3$ which agrees reasonably well with Eq. (44). Fig 1. shows that after propagating $ct = 0.32$ mm nearly half of the laser pulse has eroded away.

In order to understand where the depleted energy has gone we plot the transverse electric field, longitudinal electric field, plasma density and the transverse vector potential

in Figs. 2a,b,c and d respectively over the entire simulation box. The sharp front of the laser excites a large plasma wake and large density spike as discussed earlier. However, not all of the depeleted energy is accounted for in this wakefield. By close examination of Fig. 2a and d, we see that there is low frequency radiation left behind the pulse. The origin of this low frequency radiation can be explained as follows. The density spike is caused by the ponderomotive force of the front of the laser. This density spike is continually pushed in front of the laser pulse. As a result the front of the laser pulse resides in a density gradient. This density gradient causes radiation to frequency downshift (photon deceleration[23]) which falls behind due to a lower group velocity. In Fig. 3a we plot the k spectrum of the transverse electric field(solid line) and the k spectrum of the transverse vector potential(dashed line) after propagating 0.32 mm. For comparison we also plot the initial laser pulse spectrum(dotted line). As expected, we see a continuum of lowered radiation resulting from photon deceleration. It is interesting to note that the low k (low frequency) spectrum of the vector potential is much higher than that of the electric field. This indicates photon conservation[17] is taking place. We can define the photon number as the field energy $E^2/2\pi$ divided by the photon energy $\hbar\omega$. If photons are conserved than $E^2/\omega = \omega a(\omega)$ must be conserved and as ω decreases the vector potential increases.

The huge longitudinal wakefields involved in this process accelerate electrons to high energies. In Fig. 3b we plot the longitudinal electron momentum p_x/mc of the particles versus x after the pulse has propagated 0.32 mm. We see that the electrons have been accelerated up to $p_x = 800mc^2$(400 Mev.) The accelerating wakefield show in Fig. 2b is found to be roughly $\frac{eE_x}{mc\omega_o} = -0.3$. The energy gains shown in Fig. 3b are in good agreement with the product of the accelerating field times this accelerating distance of $1000c/\omega_o$. We note that the first peak in the wakefield of $\frac{eE_x}{mc\omega_o} = +2$ is from the space charge of the bunched electrons. This field accelerates electrons in the negative

x direction and is responsible for the return current seen in Fig. 3c. Finally, we plot the transverse electron momentum p_z/mc versus x in Fig. 3d which shows that the low frequency radiation generated results in low frequency transverse currents left behind the pulse.

We comment that local pump depletion of the leading edge of the pulse is probably an important element for the explanation of the 1-D soliton solution of Kaw et al.[24]. In their solution the radiation consisted of a high frequency mode and a low frequency mode and the pulse length is equal to the wakes nonlinear wavelength. In Fig. 6.2h the eventual generation of a low frequency peak is apparent. The low frequency component is generated by the local pump depletion which immediately transforms high frequency photons to low frequency photons with photon number being conserved. In the soliton solutions the low frequency photons must then be upshifted via photon acceleration by a density spike at the back of the pulse. Determining whether 1-D solitons can be self-consistently generated in PIC simulations is obviously an area for future research.

We next present Results from a 2-D simulation. The system size is $x_{max} = 500c/\omega_o$ and $y_{max} = 500c/\omega_o$ and the laser parameters are identical to the one dimensional simulation with a gaussian spot size of $\sigma = 25c/\omega_o$ which for a $1\mu m$ laser correspond to $4\mu m$ spot. We chose such a narrow beam in order to examine the most dramatic 2-D effects such as diffraction and ponderomotive blowout(electron expulsion).

We plot the transverse electric field associated with the laser, the longitudinal electric field and the electron density versus x for $y = 250c/\omega_p$ and $ct = 0.32$ mm in Figs. 4a,b and c respectively. We see that pulse erosion, similar to the 1-d case, has occurred and has generated density compression Fig. 4b. The velocity of the front from this 2-D simulation is also found to be $(1-v_f)\frac{\omega_o^2}{\omega_p^2} = 1.3$. However, comparison of Fig. 4b with Fig. 2b indicates that the density compressions are different. The magnitude of the density

compression is less for the 2-D case than it is for the 1-D case. This is due to the fact that the ponderomotive force has a y component at the front which can push electrons sidewise. This sideways ponderomotive force leads to complete electron expulsion for the main body of the pulse. The expelled electrons rush in behind the pulse which results in the additional density spikes shown in Fig. 4c. This will become more evident when we show 2-D density contours. Since the electron compression is less the resulting wakefield is less in 2-D than it is for 1-D.

To fully illustrate the 2-d evolution, we plot contours of $|E_z|$ and the electron density at various times in Figs. 5 and 6 respectively. We note that for the given spot size the Rayleigh length is 0.05 mm and the ratio of the power to the critical power[9] for self focusing is $P/P_c > 78$. The maximal values of $|E_z|$ at the various times indicate that self focusing is occurring.In addition, Fig. 5 shows that the laser pulse has developed a square shaped front from leading edge erosion. At lower intensities, the leading c/ω_p of the pulse always diffracts[18] even if $P/P_c > 1$. Fig. 5 indicates that the leading edge erosion occurs faster than the leading edge diffraction. The main body of the laser pulse is self focused and has propagated over 6 Rayleigh lengths. However, Figs. 5b and c show that the pulse has broken up. Unlike the low intensity , this break up is not from Raman forward scattering but from enhanced diffraction as a result of the non-linear plasma wave wake. When a plasma wave gets very nonlinear, the density compression acts like a diverging lens and causes diffraction. This localized diffraction breaks the pulse into bullet-like structures spaced at the nonlinear plasma wavelength. The density contours show total ponderomotive blow out(electron expulsion) with very complicated structures. In Fig. 6. we see that the "bullet" resides in a completely self-generated density hole. Once this bullet hole structure develops the pulse continues to propagate until the pulse completely erodes.

In Fig. 7 we plot the Fourier spectrum of $|E_z|$ at $ct = 0.32$ and 0.64 mm. We do not see any of the spectral cascading at the lower intensities described Ref. [4, 7, 10]. There are some indications of sidescattering. However, this scattering is coming from regions in the pulse which are not in the density depression and therefore the side scattering is a very small fraction of the total light. As in the one dimensional case, low frequency radiation is generated.

VI. CONCLUSIONS

In this paper we have shown that the evolution of ultra-intense laser pulses is dominated by leading edge erosion. Associated with this erosion is the excitation of large amplitude plasma waves and large amplitude density perturbations (spikes). The effects of Raman forward scattering (and related instabilities) are shown to be drastically reduced. We presented one dimensional simulation results which demonstrated this leading edge erosion. We presented results from two dimensional simulations which also show this behavior with additional effects such as plasma blow out and refraction.

We note that this behavior can be used to generate short wavelength radiation by reflecting counter propagating light off the large amplitude density spikes. These density spikes have been shown to move at relativistic speeds and can serve as moving mirrors.

In addition, the resulting plasma waves can accelerate electrons to multi-Mev energies. Simulations show that the electric fields of the plasma waves may be 4-5 times wavebreaking amplitude. Assuming a density of $n = 4 \times 10^{19} cm^{-3}$ gives an accelerating gradient of $10 TeV/m$. This mechanism may be useful as a very compact low beam quality particle accelerator.

We acknowledge useful conversations with Drs. E. Eseray, P. Sprangle, J. Krall T. Johnston and G. Shvets. Work was supported by Department of Energy Contract Nos. DE-FG0392ER40727 and DE-FG03-93ER40776 and Lawrence Livermore National

Laboratory Task Nos. 20 and 32.

References

[1] T.M. Antonsen Jr. and P. Mora, Phys. Rev. Lett. 69,2204 (1992); T.M. Antonsen Jr. and P. Mora, Phys. Fluids B 5,1440 (1993).

[2] P. Sprangle, E. Esarey, J. Krall and G. Joyce, Phys. Rev. Lett., 69, 2200 (1992).

[3] W.B. Mori, C. Decker, T. Katsouleas, and D. E. Hinkel, Phys. Rev. Lett. 72, 1482 (1994).

[4] C.Decker, W.B. Mori, and T. Katsouleas, Phys. Rev. E 50, R3338 (1994).

[5] E. Esarey, J. Krall, and P. Sprangle, Phys. Rev. Lett., 72, 2887 (1994).

[6] G. Shvets and J. Wurtele Phys. Rev. Lett.73, 3540 (1994); P. Sprangle, J. Krall and E. Esarey, Phys. Rev. Lett.73, 3544 (1994).

[7] C. A. Coverdale, C. B. Darrow, C. D. Decker, W. B. Mori, K. Marsh and C.Joshi Phys. Rev. Lett.74, 4659 (1995); Monot *et at.*, Phys. Rev. Lett. 74, 2953 (1995); Nakajima *et at.*, Phys. Rev. Lett. 74, 4428 (1995); A. Modena *et at.*, to appear in Nature.

[8] D. W. Forslund *et at.*, Phys. Rev. Lett. 54,558 (1985)

[9] C.E. Max, J. Arons, and A. B. Langdon, Phys. Rev. Lett. 33.

[10] K-C Tzeng, W. B. Mori, and C.D. Decker (submitted to Phys. Rev. Lett.)

[11] C.Decker and W.B. Mori,Phys. Rev. Lett. 72,490 (1994); C.Decker and W.B. Mori, Phys. Rev. E 51, 1364(1995).

[12] C.Decker,W.B. Mori, T. Katsouleas, and D. E. Hinkel,(submitted to phys. of plasmas)

[13] C.Decker, Phd. Thesis

[14] A.I. Akhiezer and R.V. Polovin J. Exptl. Theoret. Phys. 47,1945 (1964) [Sov. Phys. JETP 20 1307 (1965)]. , Soviet Phys. JETP, 3,696 (1956).

[15] C.J. Mckinstrie and R. Bingham, Phys. Fluids. B 4, 2626 (1992)

[16] D. W. Forslund, J. M. Kindel, and E. Lindman, Phys. Fluids, 8, 1002 (1975); J. F. Drake, P. Kaw, Y. Lee., G. Schmidt, C. Liu, and M. Rosenbluth, Phys. Fluids, 4, 1002 (1974); K. Estabrook and W.L. Kruer, Phys. Fluids, 26, 1892 (1983)

[17] S.V. Bulanov, I.N. Inovenkov, N.M. Naumova, A.S. Sakharovand Phys. Fluids B 4,1935 (1992).

[18] . P. Sprangle, E. Esarey, and A. Ting, Phys. Rev. A 41,4463 (1990); P. Sprangle, E. Esarey, and A. Ting, Phys. Rev. Lett. 64,2011 (1990).

[19] H. Goldstein, *Classical mechanics*, (Addison-Wesley, New York, 1980), p555

[20] V.I. Berezhiani and I.G. Murusidze, Phys. Lett. A 27,338 (1990).

[21] S.V. Bulanov, V.I. Kirsanov, N.M. Naumova, A.S. Sakharov and H.A. Shah, Physica Scdripta 47,209 (1992).

[22] R.L. Morse and C.W. Nielson, Phys. Fluids, 14, 830 (1971)

[23] S.C. Wilks, J. Dawson, and W. Mori, Phys. Rev. Lett., 69, 1383 (1992)

[24] P.K. Kaw, A.Sen and T. Katsouleas, Phys. Rev. Lett.68,3172 (1993).

Figure Captions

Figure 1: Results from a 1-D simulation with $a_o = 10.0$, $\omega_o/\omega_p = 5.0$ and $l_o = 125c/\omega_o$. Transverse electric field $\frac{eE_z}{m\omega_o c}$ versus $x - ct$ at $ct = 0.08$, 0.16, 0.24 and 0.32 mm.

Figure 2: a) Transverse electric field $\frac{eE_z}{m\omega_o c}$ b) longitudinal electric field $\frac{eE_x}{m\omega_o c}$ c) electron density $\frac{n}{n_o}$ and c) vector potential $\frac{eA_z}{m\omega_o c^2}$ versus x for ct=0.32 mm from 1-D simulation

Figure 3: a) K-spectrum of transverse electric field $\frac{eE_z}{m\omega_o c}$ (solid line) and transverse vector potential $\frac{eA_z}{m\omega_o c}$(dashed line) for $ct = 0.32$ mm from 1-D simulation. For comparison we also plot the initial laser pulse spectrum(dotted line). b) Longitudinal electron momentum p_x/mc^2 and c) transverse electron momentum p_x/mc^2 versus $x - ct$.

Figure 4: 2-D simulation results with $a_o = 10.0$, $\omega_o/\omega_p = 5.0$, $l_o = 125c/\omega_o$ and $r_o = 25c/\omega_o$. a) Transverse electric field $\frac{eE_z}{m\omega_o c}$ b) electron density $\frac{n}{n_o}$ for $y = 250c/omega_o$ and ct=0.32mm.

Figure 5: Contours of $|E_z|$ from 2-D simulation at a) ct=0.0mm, b) ct=0.16 mm c) ct=0.32 mm and d) ct=0.64 mm. Peak values of $|\frac{eE_z}{m\omega_o c}|$ are given in lower right hand corner of each plot.

Figure 6: Contours of electron density from 2-D simulation at a) ct=0.32 mm and b) ct=0.64 mm.

Figure 7: 2-D k-spectrum from 2-D simulation for a) ct=0.32 mm and b) ct=0.64 mm

Fig. 1

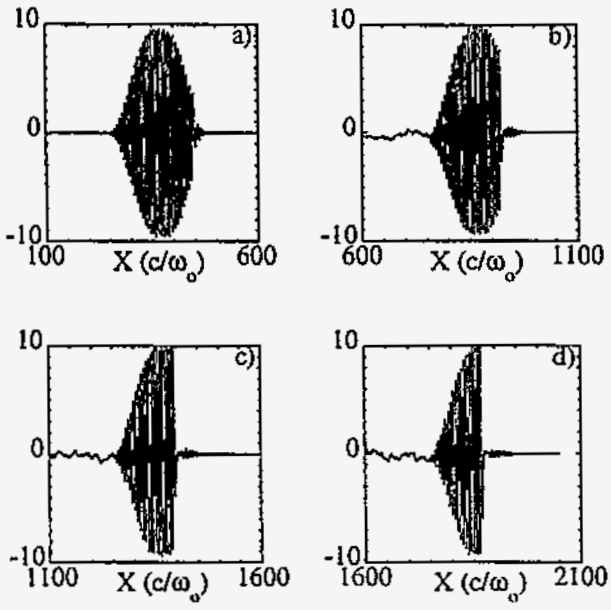

Fig. 2

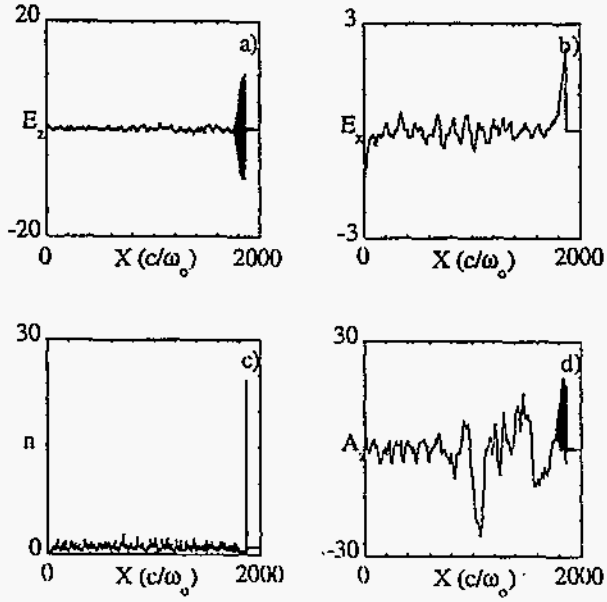
20
a)
E_z
-20
0
X (c/ω_o)
2000
3
b)
E_x
-3
0
X (c/ω_o)
2000
30
c)
n
0
0
X (c/ω_o)
2000
30
d)
A
-30
0
X (c/ω_o)
2000

Fig. 3

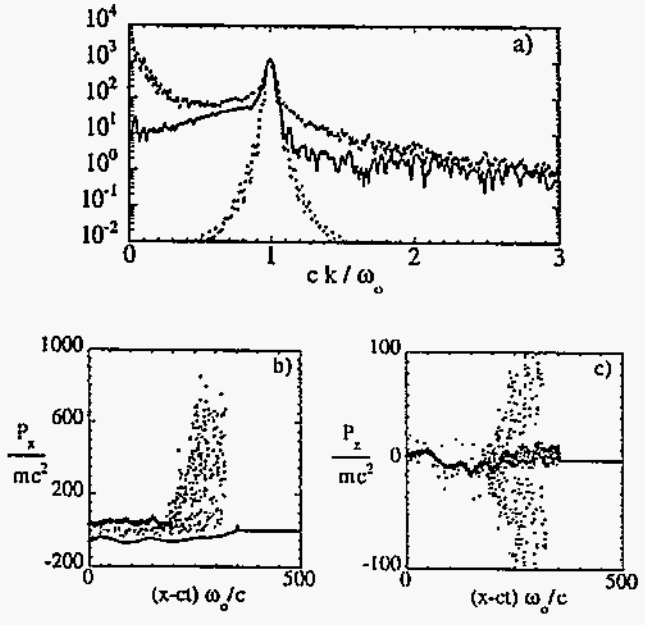
a)
10^4
10^3
10^2
10^1
10^0
10^{-1}
10^{-2}
0
1
2
3
c k / ω$_o$
b)
1000
600
200
-200
$\frac{P_x}{mc^2}$
0
500
(x-ct) ω$_o$/c
c)
100
0
-100
$\frac{P_z}{mc^2}$
0
500
(x-ct) ω$_o$/c

Fig. 4

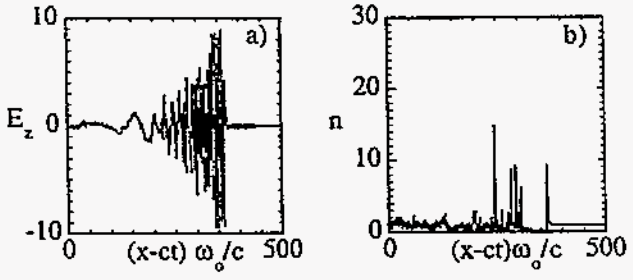

Fig. 5

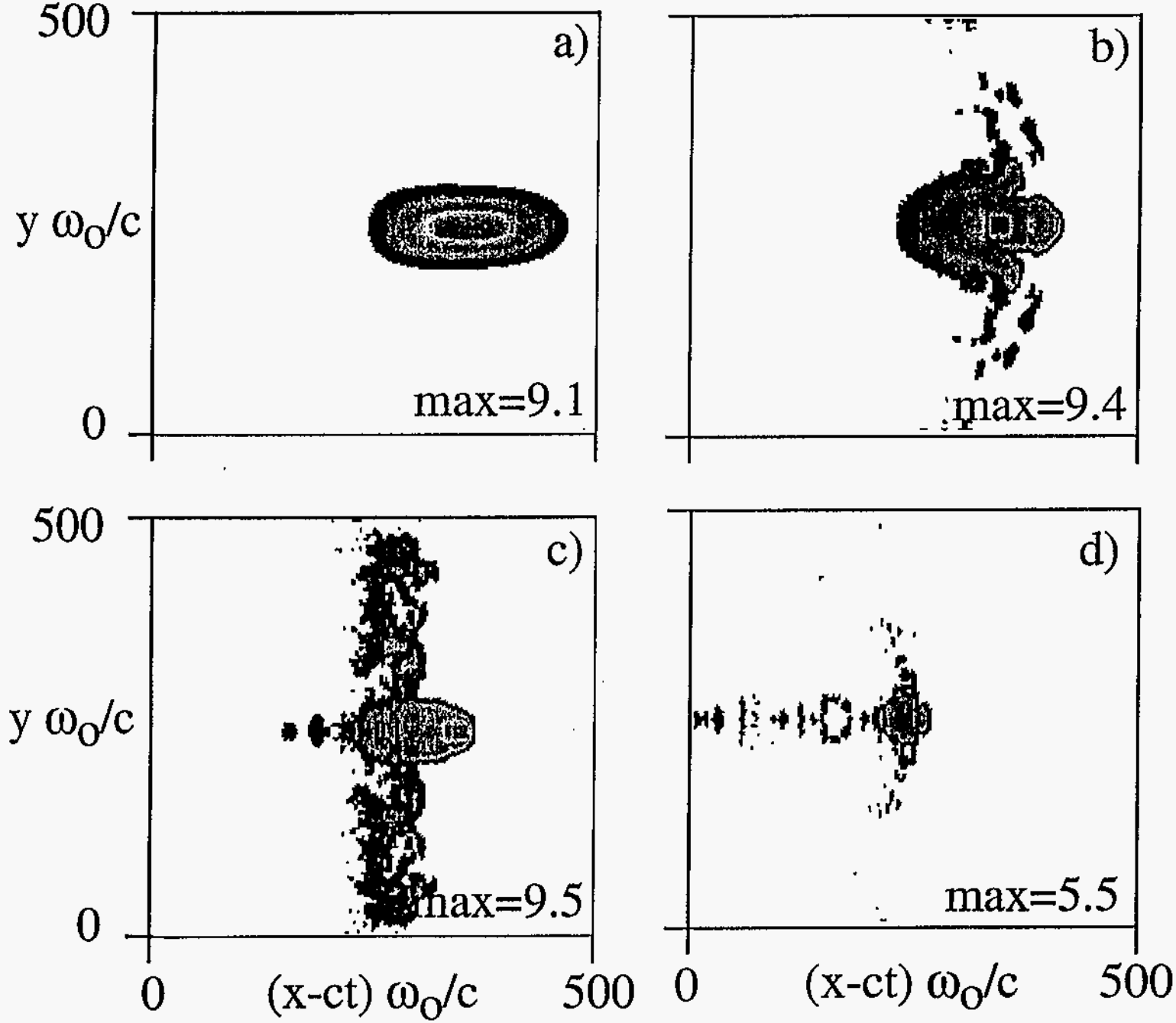
500
a)
y ω_o/c
0
max=9.1
b)
max=9.4
500
c)
y ω_o/c
0
max=9.5
d)
max=5.5
0
(x-ct) ω_o/c
500
0
(x-ct) ω_o/c
500

Fig. 6

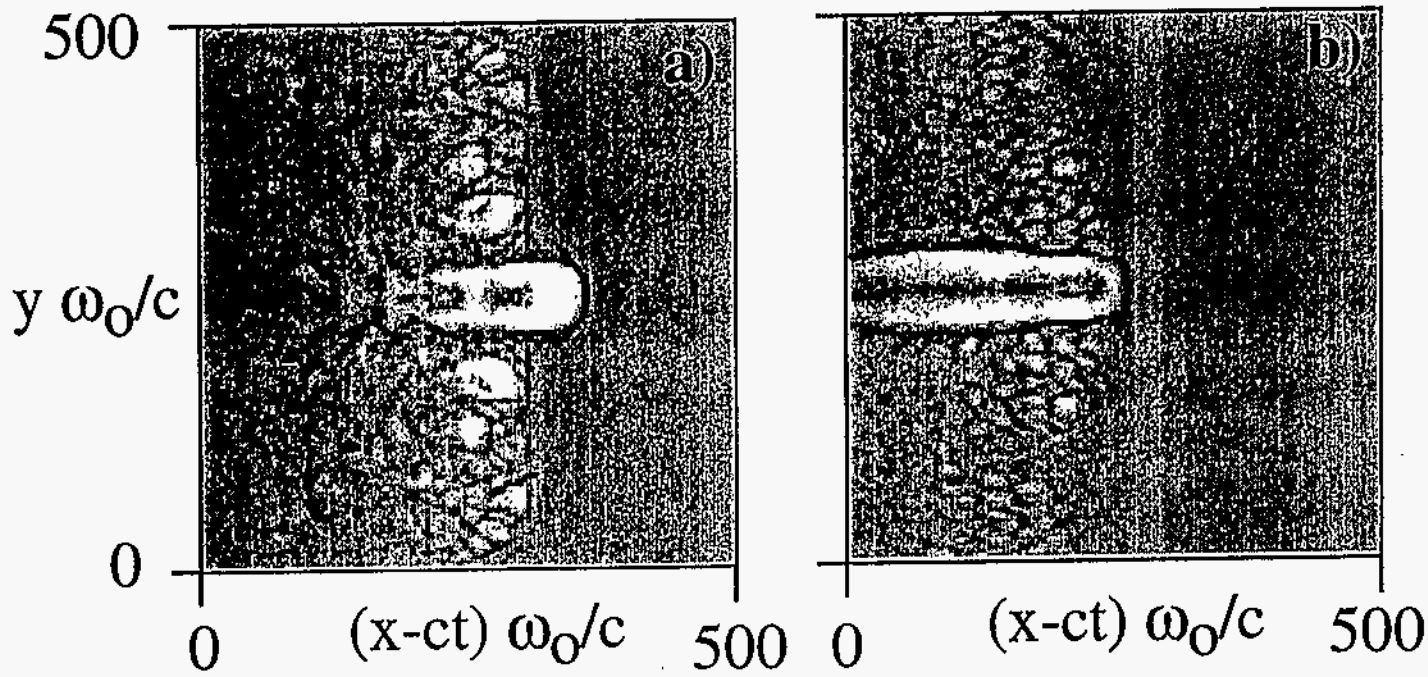

Fig. 7

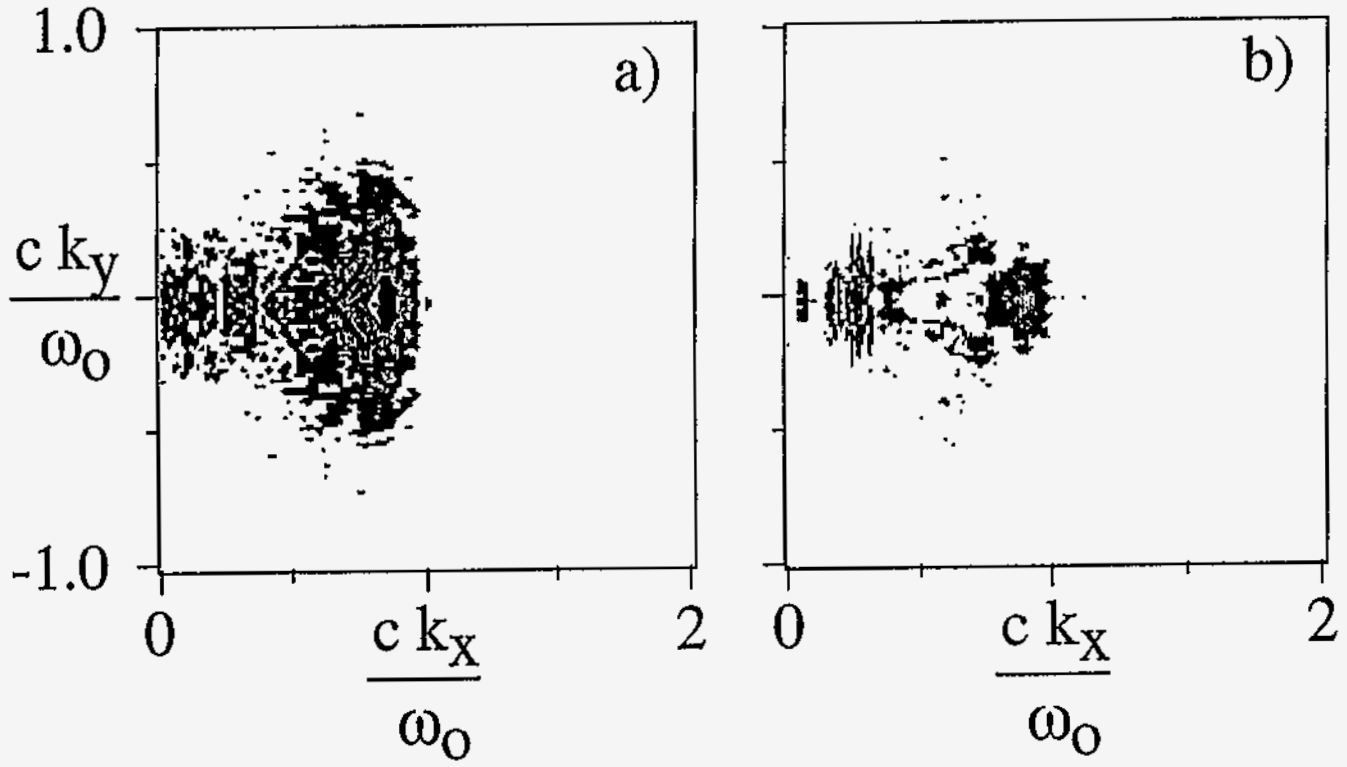

Technical Information Department • Lawrence Livermore National Laboratory
University of California • Livermore, California 94551